Bounding Higher Order Ionosphere Errors for the Dual Frequency GPS User

Seebany Datta-Barua, Todd Walter, Juan Blanch, Per Enge, *Stanford University*

ABSTRACT

The advent of a second civil GPS frequency heralds a new phase of GPS performance. For single-frequency GPS users, the signal delay due to refraction through the ionosphere is the largest and most variable source of positioning error. Dual-frequency users take advantage of the dispersive nature of the ionosphere, combining the GPS observables to eliminate most of this error, on the order of meters, introduced into the pseudoranges. Thus it is with great anticipation that we await the improved accuracy afforded by L2, and for the aviation community, L5.

However, with a second civil frequency, the ionospheric error will not disappear completely. Current techniques for measurement and removal of ionosphere delay using L1 and semi-codeless tracking of L2 typically assume a first-order approximation of the index of refraction in the ionosphere. This approximation results in a range delay inversely proportional to the square of the signal frequency, and equal and opposite to the phase advance. Once this correction is made, higher order terms are then the largest ionosphere error.

This paper examines the magnitude of these higher order ionospheric error terms. Previous analyses from the early 1990s used simulations to show that typical higher-order terms should be "much less than 1% of the first order term at GPS frequencies" (Klobuchar 1996). We verify such values with L1-L2 dual-frequency GPS data from the current solar cycle, made available by the Wide Area Augmentation System (WAAS) network. We compare the magnitude of the second and third order terms.

We assume the International Geomagnetic Reference Field IGRF-10 (10^{th} generation, created 2005) and take its value at 350 km shell height. For the third order term involving the square of the electron density, we use a technique from Hartmann and Leitinger (1984) to approximate the ionosphere vertical profile with a maximum density Nm and a shape factor. We choose a shell model with 100 km thickness and compute the uniform density consistent with WAAS equivalent vertical delay measurements as Nm, giving a shape factor of one.

We find that the Brunner & Gu (1991) model is the simplest one that neglects the sub-millimeter terms, and use this to compute the higher order group and phase errors that occur from the use of the observable that is ionosphere-free to first order (FOIF). During the most active of these days, when ionospheric storms may introduce slant range delays at L1 as high as one hundred meters, the higher order group errors in the FOIF combination can be tens of centimeters.

Moreover, the group and phase errors are no longer equal and opposite, so these errors accumulate in carrier smoothing of the FOIF code observable. We show the errors in the carrier-smoothed code are due to higher order group errors and, to a lesser extent, to higher order phase rate errors. For many applications, this residual error is sufficiently small as to be neglected. However, such errors can impact geodetic applications as well as the error budgets of Augmentation Systems providing Category III precision approach.

INTRODUCTION

The ionosphere is a weakly-ionized plasma layer of the upper atmosphere from about 60 – 1000 km. As a dispersive medium, the ionosphere advances the phase and delays the code of the GPS ranging signals in a frequency-dependent way as they travel through it. These result in errors in the code P1 and P2 and carrier phase measurements L1 and L2 made by the user:

$$P1 = \rho + I_{\rho 1}$$
$$P2 = \rho + I_{\rho 2}$$
$$L1 = \rho + I_{\phi 1} + n_1\lambda_1$$
$$L2 = \rho + I_{\phi 2} + n_2\lambda_2$$

Equation 1

In these expressions, ρ includes the true range and all non-dispersive errors such as troposphere, satellite clock bias, and receiver clock bias. The ionosphere errors are

denoted I. The carrier measurements are each ambiguous by an integer n number of wavelengths λ. The interfrequency biases are not shown. The error I due to the signal passage through the ionosphere is:

$$I = \int_{rx}^{sv} (n-1)\, d\ell$$

Equation 2

The index of refraction n that is integrated in Equation 2 is unique to each of the four GPS observables. The following section introduces these indices.

The phase index of refraction for the ionosphere is given by the Appleton-Hartree equation (shown in Equation 49 of the Appendix). By neglecting curvature and path differences for the L1 and L2 frequencies, we integrate Equation 2 along the line of sight (LOS) between the satellite sv and receiver rx. The Appleton-Hartree equation is most commonly simplified to a first order approximation. The first order model is inversely proportional to the square of the frequency and is proportional to the total electron content along the line of sight (see Appendix). Terms with higher orders of frequency can be retained for higher accuracy, and various approximations have been made in the literature to arrive at the following expression:

$$n_\phi = 1 - \frac{1}{2}X - \frac{1}{2}XY\cos\theta_B - \frac{1}{8}X^2 - \frac{1}{4}XY^2\cos^2\theta_B - \frac{1}{4}XY^2$$

Equation 3

The definitions of the variables and derivation of the expression are provided in the Appendix. Notably, Y is inversely proportional to the wave frequency f, and X is inversely proportional to the square of the frequency (Equation 50). This implies that the second term goes as $1/f^2$, the third term as $1/f^3$, and the last three terms as $1/f^4$. It is also worth pointing out that X is proportional to the electron density Ne, and that Y is proportional to the magnitude of the geomagnetic field B_0. The angle between the magnetic field and the wave propagation direction is θ_B.

The first order model of the ionosphere, the one most commonly used by dual frequency users, includes the first two terms only. Brunner and Gu (1991) retain the first four terms by order of magnitude considerations. Tucker and Fannin (1968) retain the first five terms by making a quasi-longitudinal approximation (i.e. $\theta \approx 0$). Both Bassiri and Hajj (1993) and Hartmann and Leitinger (1984) show the full Equation 3. However, Bassiri and Hajj (B&H) then reduce their model to the Brunner and Gu (B&G) model for the purposes of analysis. The derivation of each of these models and the approximations made to arrive at them are provided in detail in the Appendix.

The group index is related to the phase index of refraction (Jackson 1999):

$$n_\rho = n_\phi + f\frac{dn_\phi}{df}$$

Equation 4

Substituting Equation 3 into Equation 4 gives group index:

$$n_\rho = 1 + \frac{1}{2}X + XY\cos\theta_B + \frac{3}{8}X^2 + \frac{3}{4}XY^2\cos^2\theta_B + \frac{3}{4}XY^2$$

Equation 5

As with the phase index, the group index is frequency-dependent through X and Y. The expression for the group index, Equation 5, may be inserted into Equation 2 to give the code range errors:

$$I_{\rho 1} = \frac{q}{f_1^2} + \frac{s}{f_1^3} + \frac{r}{f_1^4}$$

$$I_{\rho 2} = \frac{q}{f_2^2} + \frac{s}{f_2^3} + \frac{r}{f_2^4}$$

Equation 6

The terms q, s, and r will be defined below. Similar substitution of the phase index of refraction shown in Equation 3 into Equation 2 gives the phase errors at L1 and L2:

$$I_{\phi 1} = -\frac{q}{f_1^2} - \frac{s}{2f_1^3} - \frac{r}{3f_1^4}$$

$$I_{\phi 2} = -\frac{q}{f_2^2} - \frac{s}{2f_2^3} - \frac{r}{3f_2^4}$$

Equation 7

In these expressions, f1=1575.42 MHz is the L1 frequency and f2=1227.60 MHz is the L2 frequency. In Equation 6 and Equation 7 we have borrowed the notation of q, s, and r from Bassiri and Hajj (B&H). The expressions for q and s can be defined in terms of the constants C_x and C_y that B&G use as follows:

$$q = \frac{C_x}{2}\int_{rx}^{sv} N_e\, dl$$

Equation 8

$$s = C_x C_y \int_{rx}^{sv} N_e B_0 \left|\cos\theta_B\right| dl$$

Equation 9

The constants C_x and C_y will be defined below. We subdivide the term B&H defined as "r" below, and define each part in terms of the constants C_x and C_y:

$$r = r_1 + r_2 + r_3$$

Equation 10

$$r_1 = \frac{3C_x^2}{8}\int_{rx}^{sv} N_e^2 dl$$

Equation 11

$$r_2 = \frac{3C_x C_y^2}{2}\int_{rx}^{sv} N_e B_0^2 (\cos^2\theta_B) dl$$

Equation 12

$$r_3 = \frac{3C_x C_y^2}{4}\int_{rx}^{sv} N_e B_0^2 dl$$

Equation 13

In each of these expressions N_e is the electron density at a point in space, B_0 is the magnitude of the geomagnetic field at that point, and $\cos\theta_B$ is the angle between the propagation direction and the magnetic field direction. The B&G constants C_x and C_y come from the constants in the plasma frequency and gyro frequency (Appendix Equation 50 and Equation 51). These are:

$$C_x = \frac{e^2}{4\pi^2 \varepsilon_0 m_e}$$

$$C_y = \frac{e}{2\pi m_e}$$

Equation 14

The constants that appear in Equation 14 are defined in the Appendix. Our analysis will isolate the effect that the higher order terms s, r1, r2, and r3 will have for a user forming the combination of the observables that are first-order-ionosphere free (FOIF), which removes only the q term:

$$L_{FOIF} = \frac{L1 - \omega L2}{1 - \omega}$$

Equation 15

$$\omega = \frac{1}{\gamma} = \frac{f_2^2}{f_1^2}$$

Equation 16

Substituting Equation 1, Equation 6, Equation 7, and Equation 16 into Equation 15, we obtain:

$$\begin{aligned} L_{FOIF} &= \frac{\rho - \frac{q}{f_1^2} - \frac{s}{2f_1^3} - \frac{r}{3f_1^4} + n_1\lambda_1}{1-\omega} \\ &\quad \frac{-\omega\left(\rho - \frac{q}{f_2^2} - \frac{s}{2f_2^3} - \frac{r}{3f_2^4} + n_2\lambda_2\right)}{1-\omega} \\ &= \rho + \frac{1}{1-\omega}\left(\frac{\omega s}{2f_2^3} - \frac{s}{2f_1^3}\right) + \frac{1}{1-\omega}\left(\frac{\omega r}{3f_2^4} - \frac{r}{3f_1^4}\right) + B \\ &= \rho + \frac{s}{2f_1 f_2 (f_1 + f_2)} + \frac{r}{3f_1^2 f_2^2} + B \end{aligned}$$

Equation 17

In this expression, the integer ambiguities have been absorbed into bias B. Klobuchar (1996) observed that both B&G and B&H predicted that the higher order phase errors (i.e. the s and r terms in Equation 17) would be on the order of 0.1% of the first order error q/f_1^2 term via simulation. Since the typical ionosphere delay at L1 frequency is on the order of 10 m, this would translate to higher order errors at the centimeter level. As Klobuchar noted, the B&G model error estimates were more accurate but required more knowledge of the state of the ionosphere and geomagnetic field. In particular they estimated curvature effects due to the signals not traveling along the straight line path, and moreover, not traveling on the same curved path. B&H neglect curvature, treating the integration as taking place along the line of sight. They additionally consider the group index of refraction and the corresponding code errors, predicting them to be at the centimeter level.

MAGNETIC FIELD MODEL

In order to estimate the higher order errors using the dual frequency GPS observables P1, P2, L1, and L2, we make a number of simplifications to Equation 9 through Equation 13. For s in Equation 9, r2 in Equation 12, and r3 in Equation 13, we need information about the magnetic field within the ionosphere. For this we assume the international geomagnetic reference field IGRF-10 (Macmillan 2005). IGRF-10 is a spherical harmonic multipole expansion of the field, with 10th generation updated estimates of the coefficients from those used by Brunner and Gu (1991) and Bassiri and Hajj (1993). The expression for the scalar potential V is (Walt 1994):

$$V = R_E \sum_{n=1}^{\infty}\left(\frac{R_E}{r}\right)^{n+1}\sum_{m=0}^{n}(g_n^m \cos m\phi + h_n^m \sin m\phi)\, P_n^m(\cos\theta)$$

$$P_n^m = \left[\frac{(n-m)!(2-\delta_{0,m})}{(n+m)!}\right]^{1/2} P_{n,m}$$

Equation 18

In this expression R_E = 6371.2 km is the radius of the earth. The variables r, θ, and φ are the spherical geographic coordinates of a point in space. The coefficients g_n^m and h_n^m are specified by the IGRF-10 model. The expression P_n^m is the Schmidt normalization of the Legendre functions $P_{n,m}$, and $\delta_{0,m}$=1 for m=0 and zero otherwise. The components of the magnetic field B are then obtained from the potential V as:

$$B_r = -\frac{\partial V}{\partial r}, \quad B_\theta = -\frac{1}{r}\frac{\partial V}{\partial \theta}, \quad B_\phi = -\frac{1}{r\sin\theta}\frac{\partial V}{\partial \phi}$$

Equation 19

In these expressions, B_r is the upward component, B_θ is the southward component, and B_φ is the eastward component of the field. Tsyganenko (2005) has made an implementation of the IGRF model publicly available as Fortran code, which we adapted for use in Matlab.

The specification of a magnetic field B_0 alone is not sufficient to allow for the calculation of the s, r2, and r3 terms, since they must be integrated against the unknown electron density distribution Ne. Since we use real data, particularly during ionospherically active times, we do not assume a Chapman function for the ionosphere, as B&G and B&H did. Therefore, we will not integrate the product of Ne and B_0. Instead, we take as average magnetic field the value of B_0 and $\cos\theta_B$ at the point where the line of sight reaches 350 km altitude (the ionosphere pierce point, IPP). This allows us to pull the $B_0\cos\theta_B$ term out of the integrals in Equation 9Equation 12Equation 13. This average value is conservative since the geomagnetic field is reduced by currents induced in the magnetosphere during ionospherically stormy times, as evidenced by negative Dst geomagnetic storm index. The use of the field value at the IPP is also conservative since evaluation at 350 km altitude treats the bulk of the electrons as being at that altitude, when in fact storm time plasma enhancements have been observed to occur at higher altitudes (Mannucci 2005), where the magnetic field is weaker.

SIMPLIFICATION OF Ne

To estimate the r1 term defined in Equation 11, which integrates the square of the electron density Ne along the line of sight, we use a technique introduced by Hartmann and Leitinger (1984). This involves the definition of a shape factor η:

$$\eta \equiv \frac{\int_{rx}^{sv} N_e^2 dl}{N_m \int_{rx}^{sv} N_e dl}$$

Equation 20

In this expression Nm is the maximum density in the vertical density profile. In the literature, since Chapman functions with specified Nm were assumed, it was found that eta was 0.66 nearly independently of elevation.

Rather than use a Chapman function, we make an assumption that is both conservative and consistent with our data. We assume the ionosphere is a shell of thickness 100 km. Then we take our dual-frequency measurements of the first order delay I_S, and convert them to equivalent vertical measurements I_V using the obliquity factor M:

$$M(el, h_{iono}) = \frac{1}{\cos\left[Sin^{-1}\left(\frac{R_E\cos(el)}{R_E + h_{iono}}\right)\right]}$$

Equation 21

The obliquity factor M is a function of the elevation el to one satellite. The height of the ionosphere h_{iono} is fixed at 350 km. The equivalent vertical delay I_V is related to a slant delay I_S as:

$$I_V = \frac{I_S}{M(el, h_{iono})}$$

Equation 22

Then Nm is given by:

$$N_m = \frac{I_V}{\tau} = \frac{I_V}{100\ km}$$

Equation 23

In other words, we compute the equivalent vertical first order delay from the slant, and then spread the electrons causing that delay evenly within a shell of thickness τ=100 km. Substituting this model of electron density Ne and maximum density Nm into Equation 20, we find that η=1. This gives a conservative value of η. Compared to the international reference ionosphere (IRI) model, in which the vast majority of electrons are typically within a band of 150-200 km thickness, a narrow shell of 100 km thickness gives a more delta-like density function, i.e. a higher value of Nm. Therefore, this assumption is conservative. A cartoon, not to scale, depicting this simplification is shown in Figure 1. It illustrates the variation of the electron density with height. An IRI model (black curve) rises to a peak and tapers off with altitude. A set of shells of varying thickness are shown as blue, green, and yellow rectangles. Each one contains the same area (i.e. the same total electron content, TEC). The blue rectangle represents a shell of thickness 100 km. This maximum density Nm associated with this choice of vertical profile is both higher than a Chapman function with the same TEC and gives a higher value of η than a

Chapman function would. Therefore, it can be used to bound the r1 error.

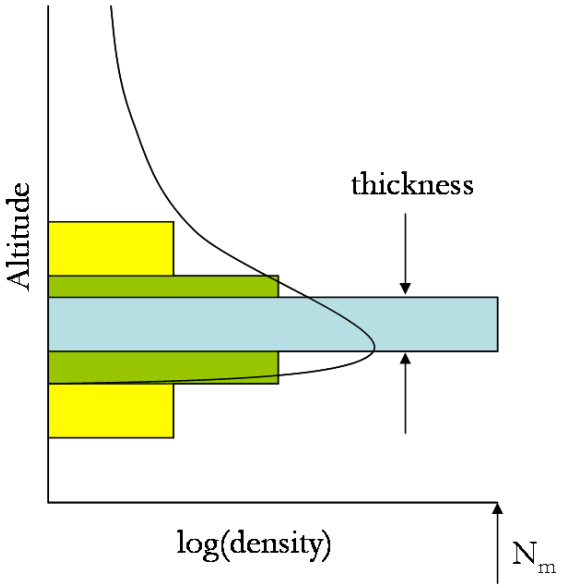

Figure 1: Illustration of vertical density profile chosen for specification of Nm and, thus, η.

HIGHER ORDER ERRORS FROM DATA

The goal of this section is to demonstrate how to extract the higher order errors from the data. We will show that, by differencing two iono-free models, each with different orders of accuracy, we can isolate those q, s, or r terms that are not common to both models.

Dual-frequency measurements allow us to directly compute the q term, or TEC, in Equation 8. The simplifications to s and r described in the previous two sections involve taking an average value of quantities inside the integrals of Equation 8-Equation 13, so that we may pull them out of the integral and express them in terms of the TEC. Using the simplifications outlined in the two sections above and factoring out the TEC, we obtain slightly modified expressions for the q, s, and r of Equation 8-Equation 13:

$$q' = \frac{C_x}{2}, \quad s' = C_x C_y \left| B\cos\theta_B \right|_{IPP}$$

$$r' = r_1' + r_2' + r_3', \quad r_1' = \frac{3C_x^2}{8} N_m \eta$$

$$r_2' = \frac{3C_x C_y^2}{2} (B\cos\theta_B)^2 \Big|_{IPP}, \quad r_3' = \frac{3C_x C_y^2}{2} B^2 \Big|_{IPP}$$

Equation 24

With this notation we bridge the gap between the q,s, and r notation that B&H use and the Ω notation of B&G:

$$\Omega_{\phi 1} = \frac{q'}{f_1^2} + \frac{s'}{2f_1^3} + \frac{r_1'}{3f_1^4}$$

$$\Omega_{\phi 2} = \frac{q'}{f_2^2} + \frac{s'}{2f_2^3} + \frac{r_1'}{3f_2^4}$$

Equation 25

By substituting Equation 25 into Equation 7, we express the ionosphere phase errors as:

$$I_{\phi 1} = -\Omega_{\phi 1} \int_{rx}^{sv} N_e dl$$

$$I_{\phi 2} = -\Omega_{\phi 2} \int_{rx}^{sv} N_e dl$$

Equation 26

From these phase errors appearing in the observables, B&G showed that an ionosphere-free phase observable L_{TOIF1} accurate through the first third-order-term r1 could be produced. The subscript TOIF1 is an acronym for "Third-Order-Ionosphere-Free through the r1 term":

$$L_{TOIF1} = \frac{L1 - \Omega_\phi L2}{1 - \Omega_\phi}$$

$$\Omega_\phi = \frac{\Omega_{\phi 1}}{\Omega_{\phi 2}}$$

Equation 27

The full expression for the B&G improved iono-free model included curvature terms, which we have omitted here. Notice that Equation 27 is similar in form to the FOIF model in Equation 15, with Ω replacing ω.

Brunner and Gu showed that the difference between the FOIF phase observable in Equation 15 and their higher order iono-free phase observable was a function of the difference between the phase measurements. We detail that derivation here, starting with the definitions of the TOIF1 model in Equation 27 and the FOIF model in Equation 15:

$$L_{TOIF1} - L_{FOIF} = \frac{L1 - \Omega_\phi L2}{1 - \Omega_\phi} - \frac{L1 - \omega L2}{1 - \omega}$$

Equation 28

This can be rearranged to obtain:

$$L_{TOIF1} - L_{FOIF} = \frac{(1-\omega) - (1-\Omega_\phi)}{(1-\Omega_\phi)(1-\omega)} L1 - \frac{\Omega_\phi(1-\omega) - \omega(1-\Omega_\phi)}{(1-\Omega_\phi)(1-\omega)} L2$$

Equation 29

Define Δω as:

$$\Delta\omega = \Omega_\phi - \omega$$

Equation 30

Then we may continue the derivation from Equation 29:

$$\begin{aligned} L_{TOIF1} - L_{FOIF} &= \frac{\Delta\omega}{(1-\omega-\Delta\omega)(1-\omega)} L1 \\ &\quad - \frac{(\omega+\Delta\omega)(1-\omega)-\omega(1-\omega-\Delta\omega)}{(1-\omega-\Delta\omega)(1-\omega)} L2 \\ &= \frac{\Delta\omega}{(1-\omega)^2 - \Delta\omega(1-\omega)} L1 \\ &\quad - \frac{\Delta\omega}{(1-\omega)^2 - \Delta\omega(1-\omega)} L2 \\ &\approx \frac{\Omega-\omega}{(1-\omega)^2}(L1-L2) \end{aligned}$$

Equation 31

The final line in Equation 31 is the expression that B&G derive. Notice that, to reach this form, the Δω term in the denominator must be discarded. In practice this limits the accuracy to the 10^{-6} m level, which is sufficient for our purposes. Differencing between two different models is useful because the data we use provides not the L1 and L2 observables separately, but the difference between them.

Next we show that this difference in the two models is equal to the error due to the higher order terms. We will show it for the comparison of the B&G model, TOIF1, to the FOIF model. The same argument then applies to any other pair of models. We begin by substituting the expressions for L1 and L2 from Equation 1 into Equation 28:

$$\begin{aligned} L_{TOIF1} - L_{FOIF} &= \frac{L1-\Omega_\phi L2}{1-\Omega_\phi} - \frac{L1-\omega L2}{1-\omega} \\ &= \frac{\rho + I_{\phi1} + n_1\lambda_1 - \Omega_\phi(\rho + I_{\phi2} + n_2\lambda_2)}{1-\Omega_\phi} \\ &\quad - \frac{\rho + I_{\phi1} + n_1\lambda_1 - \omega(\rho + I_{\phi2} + n_2\lambda_2)}{1-\omega} \end{aligned}$$

Equation 32

Then we substitute in the expressions for the ionosphere error from Equation 26 and rearrange:

$$\begin{aligned} L_{TOIF1} - L_{FOIF} &= \rho + \frac{-\Omega_{\phi1}\int_{rx}^{sv} N_e dl + \Omega_\phi\Omega_{\phi2}\int_{rx}^{sv} N_e dl}{1-\Omega_\phi} \\ &\quad + \frac{n_1\lambda_1 - \Omega_\phi n_2\lambda_2}{1-\Omega_\phi} - \rho + \frac{I_{\phi1} - \omega I_{\phi2}}{1-\omega} \\ &\quad - \frac{n_1\lambda_1 - \omega n_2\lambda_2}{1-\omega} \end{aligned}$$

Equation 33

The range plus non-dispersive terms ρ cancel out. Since Ω_ϕ is simply the ratio of $\Omega_{\phi1}$ and $\Omega_{\phi2}$, the second term vanishes. The difference between the integer ambiguity terms is very small since Ω - ω is small, so we neglect it. After substituting in Equation 7, we are left with:

$$\begin{aligned} L_{TOIF1} - L_{FOIF} &= \frac{-\frac{q}{f_1^2} - \frac{s}{2f_1^3} - \frac{r_1}{3f_1^4}}{1-\frac{f_2^2}{f_1^2}} \\ &\quad + \frac{\frac{f_2^2}{f_1^2}\left(\frac{q}{f_2^2} + \frac{s}{2f_2^3} + \frac{r_1}{3f_2^4}\right)}{1-\frac{f_2^2}{f_1^2}} \\ &= -\frac{s}{2f_1f_2(f_1+f_2)} - \frac{r_1}{3f_1^2f_2^2} \end{aligned}$$

Equation 34

This shows that the difference between any two orders of models will depend on the terms that are included in one but not the other. This works for any two orders of phase models, and it works for any two orders of group models.

We extend this technique to isolate the effect of each individual term of the expansion. Therefore, we must difference two models of consecutive orders of accuracy. For example, to estimate the error in an iono-free observable due to the 2nd order term (namely the s term in Equation 7) we form a second-order-iono-free (SOIF) observable following the same procedure as outlined for the B&G model in Equation 25-Equation 27. The only difference is that we truncate $\Omega_{\varphi i}$ in Equation 25 to keep only the first and second order terms, q and s. Equation 15 is the FOIF observable. By differencing the two we isolate the contribution of the s term to the FOIF model phase error:

$$L_{SOIF} - L_{FOIF} = -\frac{s}{2f_1 f_2 (f_1 + f_2)} = \frac{\Omega_s - \omega}{(1-\omega)^2}(L1 - L2)$$

Equation 35

In this expression the subscript on Ω indicates the highest order term included in the model. By similar technique of differencing the TOIF1 model (which accounts for q, s, and r1) from the SOIF model (which includes only q and s), we isolate r1:

$$L_{TOIF1} - L_{SOIF} = -\frac{r_1}{3f_1^2 f_2^2} = \frac{\Omega_{r1} - \Omega_s}{(1-\Omega_s)^2}(L1 - L2)$$

Equation 36

Likewise, we form an observable that accounts for q, s, and the two third-order terms r1 and r2 in the expression for Ω in Equation 25. This observable is iono-free up to the second third order term (TOIF2). Differencing from the TOIF1 observable isolates the effect of r2:

$$L_{TOIF2} - L_{TOIF1} = -\frac{r_2}{3f_1^2 f_2^2} = \frac{\Omega_{r2} - \Omega_{r1}}{(1-\Omega_{r1})^2}(L1 - L2)$$

Equation 37

In the same way, the effect of r3 is given by:

$$L_{TOIF3} - L_{TOIF2} = -\frac{r_3}{3f_1^2 f_2^2} = \frac{\Omega_{r3} - \Omega_{r2}}{(1-\Omega_{r2})^2}(L1 - L2)$$

Equation 38

A similar technique may be applied to the group (i.e. code) errors. However, it is simpler to extend the phase model results, as we will show. The model of the range that is ionosphere-free to first order (FOIF) is:

$$P_{FOIF} = \frac{P1 - \omega P2}{1-\omega} = \rho - \frac{s}{f_1 f_2 (f_1 + f_2)} - \frac{r}{f_1^2 f_2^2}$$

Equation 39

In this expression ω is given by Equation 16. Notice that the s terms in Equation 17 and Equation 39 differ by a factor of -2. This means that the errors due to the s term in the first-order-iono-free (FOIF) code observable will be the double those of the phase error shown in Equation 39, and opposite in sign. Similarly, the r terms in those same equations differ by a factor of -3. Therefore, errors in the FOIF code observable due to the r terms will be triple the magnitude (and opposite in sign) of the errors given by Equation 36-Equation 38.

As a complement to the B&G carrier phase model of Equation 25 and Equation 27, we specify the corresponding code observable that is iono-free up to the first third-order term (TOIF1):

$$P_{TOIF1} = \frac{P1 - \Omega_\rho P2}{1 - \Omega_\rho}$$

$$\Omega_\rho = \frac{\Omega_{\rho 1}}{\Omega_{\rho 2}}$$

Equation 40

$$\Omega_{\rho 1} = \frac{q'}{f_1^2} + \frac{s'}{f_1^3} + \frac{r_1'}{f_1^4}$$

$$\Omega_{\rho 2} = \frac{q'}{f_2^2} + \frac{s'}{f_2^3} + \frac{r_1'}{f_2^4}$$

Equation 41

The s term differs by a factor of 2, and the r1 term differs by a factor of 3. The ionosphere error on the code (corresponding to the carrier error of Equation 26) is:

$$I_{\rho 1} = \Omega_{\rho 1} \int_{rx}^{sv} N_e dl$$

$$I_{\rho 2} = \Omega_{\rho 2} \int_{rx}^{sv} N_e dl$$

Equation 42

DATA

Given the observable L1-L2, we now have a method, shown in Equation 35-Equation 38, to isolate each of the error terms that will result from the use of the first-order-iono-free (FOIF) expression. We apply Equation 35-Equation 38 to the FAA's Wide Area Augmentation System (WAAS) network dual frequency measurements, known as supertruth data.

WAAS supertruth data consists of post-processed dual-frequency measurements of the first-order ionosphere delay, formed as:

$$I_S = \frac{L1 - L2}{\gamma - 1}$$

Equation 43

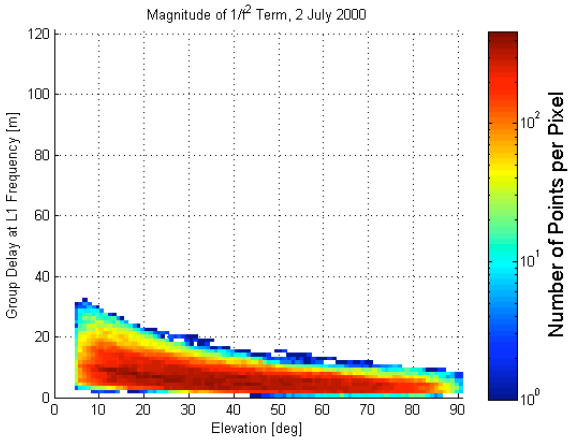

Figure 2: First order phase advance (or group delay) q ~ Ne/f^2, quiet day. Y-axis scale: 0-120 m.

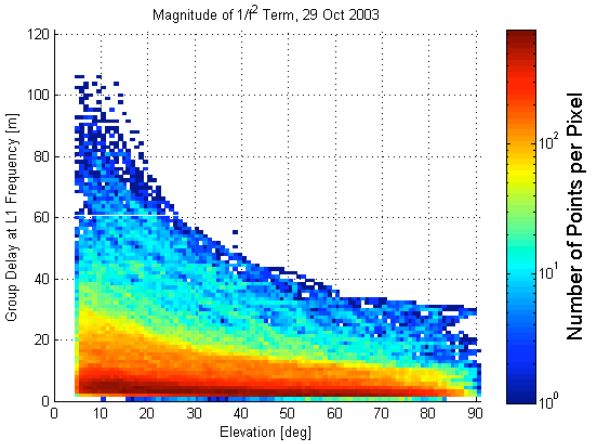

Figure 5: First order phase advance (or group delay) q ~ Ne/f^2, active day. Y-axis scale: 0-120 m.

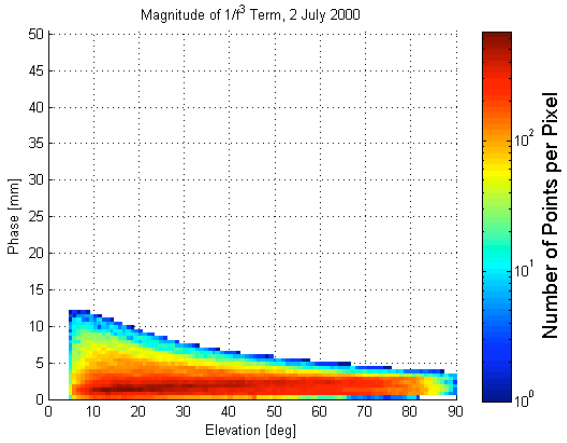

Figure 3: Second order phase advance (a.k.a ½ group delay) s ~ $NeB_0\cos\theta_B/f^3$, quiet day. Y-axis scale: 0-50 mm.

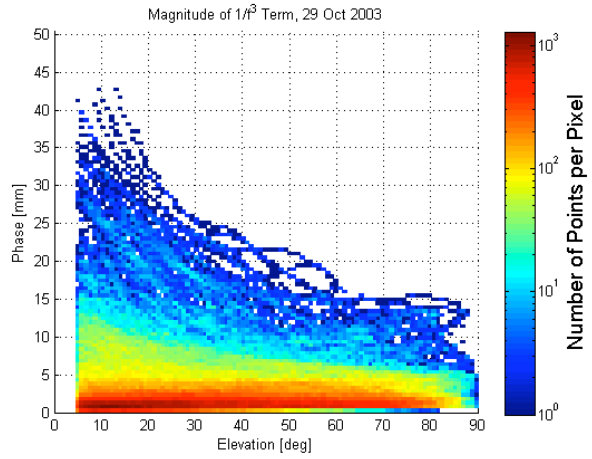

Figure 6: Second order phase advance (a.k.a ½ group delay) s ~ $NeB_0\cos\theta_B/f^3$, active day. Y-axis scale: 0-50 mm.

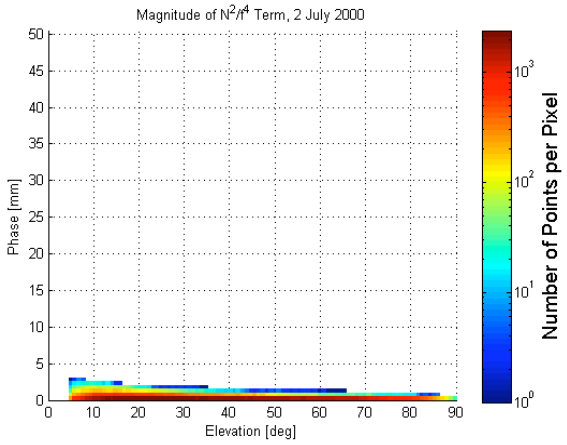

Figure 4: Third order phase advance (a.k.a $^1/_3$ group delay) r1 ~ Ne^2/f^4, quiet day. Y-axis scale: 0- 50 mm.

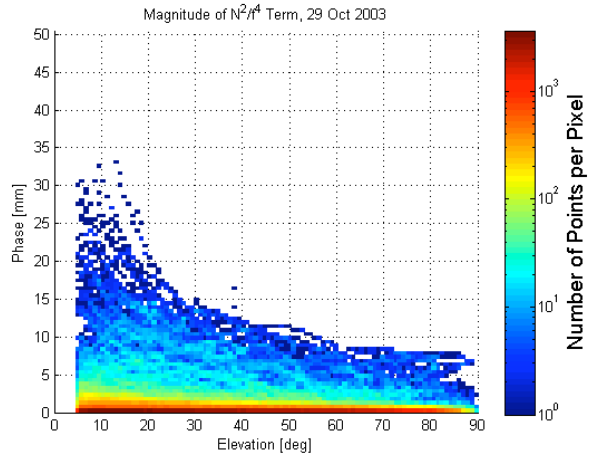

Figure 7: Third order phase advance (a.k.a $^1/_3$ group delay) r1 ~ Ne^2/f^4, active day. Y-axis scale: 0-50 mm.

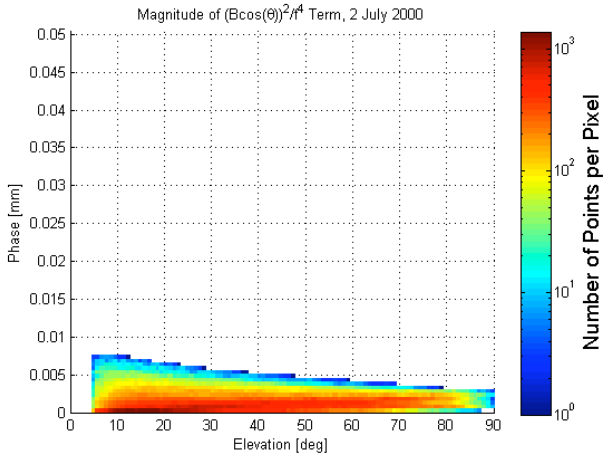

Figure 8: Third order phase advance (a.k.a $^1/_3$ group delay) r2 ~ $Ne(B_0\cos\theta_B)^2/f^4$, quiet day. Y-axis scale: 0-0.05 mm.

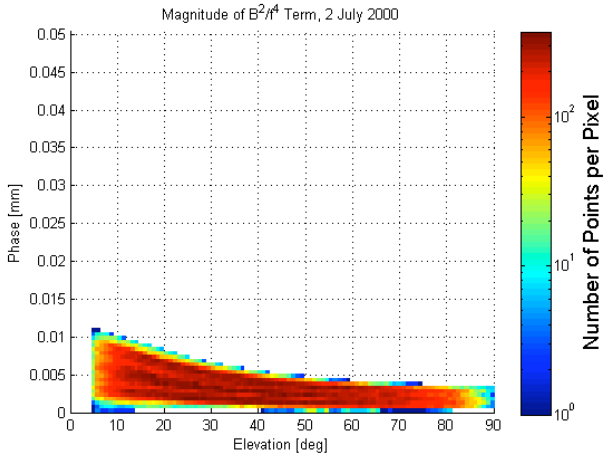

Figure 9: Third order phase advance (a.k.a $^1/_3$ group delay) r3 ~ NeB_0^2/f^4, quiet day. Y-axis scale: 0-0.05 mm.

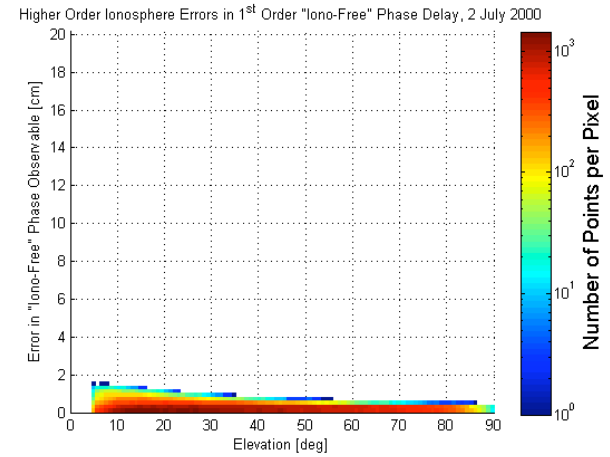

Figure 10: Total higher order phase advance, quiet day. Y-axis scale: 0-20 cm.

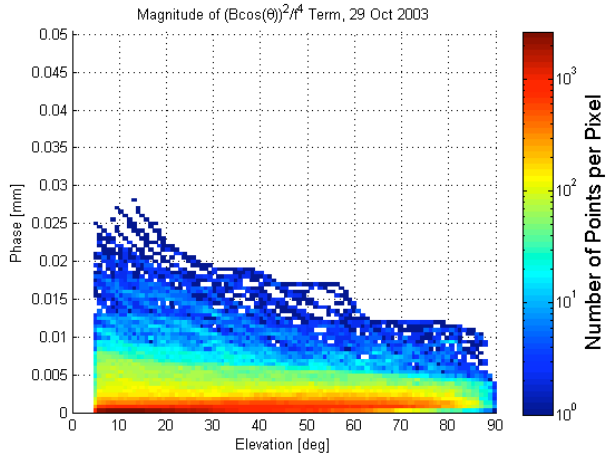

Figure 11: Third order phase advance (a.k.a $^1/_3$ group delay) r2 ~ $Ne(B_0\cos\theta_B)^2/f^4$, active day. Y-axis scale: 0-0.05 mm.

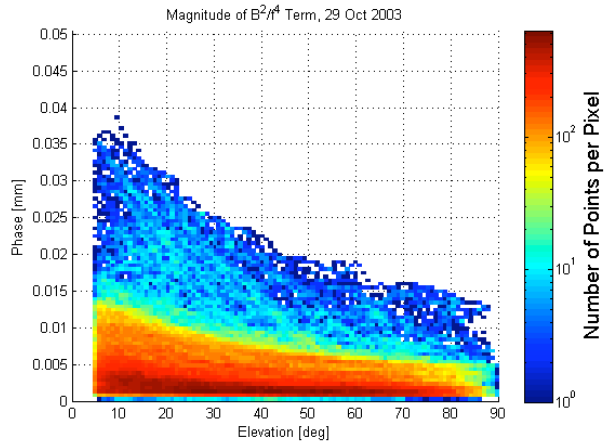

Figure 12: Third order phase advance (a.k.a $^1/_3$ group delay) r3 ~ NeB_0^2/f^4, active day. Y-axis scale: 0-0.05 mm.

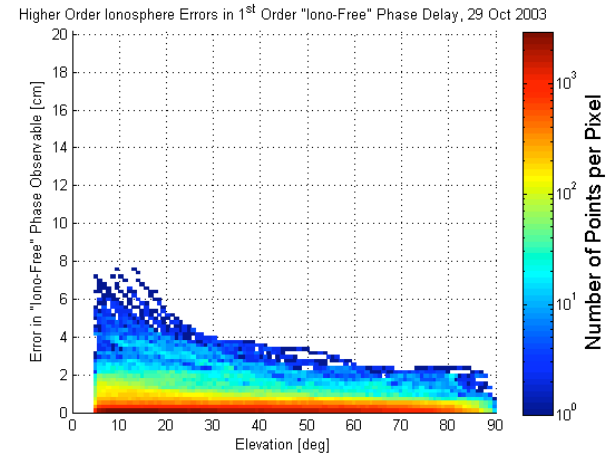

Figure 13: Total higher order phase advance, active day. Y-axis scale: 0-20 cm.

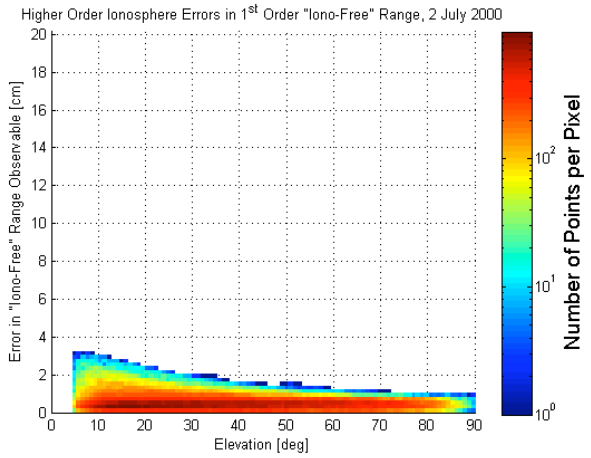

Figure 14: Total higher order group delay, quiet day. Y-axis scale: 0-20 cm.

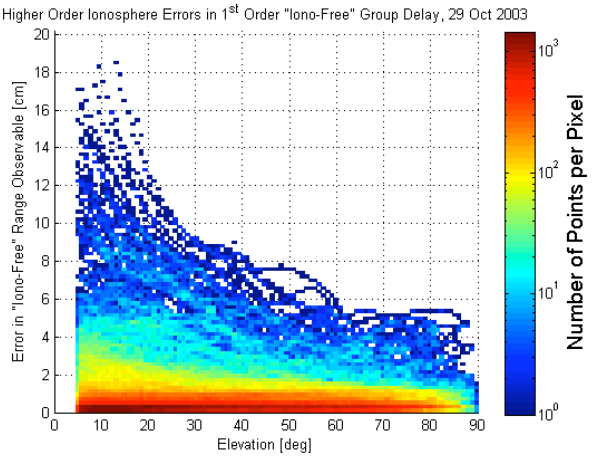

Figure 15: Total higher order group delay, active day. Y-axis scale: 0-20 cm.

The constant γ is defined in Equation 16 and the mapping function M(el) is defined in Equation 21. These dual-frequency carrier measurements are leveled to the code measurements to remove the integer ambiguities. The inter-frequency biases are estimated, and a voting system among the three receivers at each station checks for consistency between the receivers.

From these measurements we can solve for the difference L1-L2 and then substitute the values of L1-L2 into Equation 35-Equation 38. We choose to estimate the higher order errors on one ionospherically quiet day, 2 July 2000, and one extremely active day, 29 October 2003. The results are shown in the figures.

Figure 2 shows a two-dimensional histogram of the magnitude of the first order ionosphere error (identical for code and carrier) on a quiet day. The delays are placed in bins according to elevation angle of the satellite in degrees (x-axis) and magnitude of the error in meters (y-axis). The color indicates the number of measurements that fall within a given elevation and error range. Figure 5 shows a corresponding histogram for an active day. On both figures, the y-axis scale ranges from 0 to 120 m. This error corresponds to the q term in Equation 6-Equation 7 and is removed by use of the dual frequency model of Equation 15. On the quiet day, first order errors range from as much as 10 m at high elevation to 30 m at low elevation. On the active day first order errors were observed to be 30 m at high elevation up to 110 m at low elevation. In both cases the errors increase with decreasing elevation since low elevation lines-of-sight pass through more ionosphere to increase the total electron content along the path length.

Figure 3 and Figure 6 are two-dimensional histograms of the second order phase error magnitude due to the ionosphere, given by Equation 35, which arises when using the first-order-iono-free model. The quiet day is shown in Figure 3, and the active day errors are in Figure 6. Notice that, unlike Figure 2 and Figure 5, the y-axis ranges from 0 to *50 mm*. On the quiet day the highest errors are 12 mm at low elevation, whereas on the active day they are as much as 45 mm. The magnitude of the second order group error is twice the values shown in Figure 3 and Figure 6.

The contribution of the r1 term, shown in Equation 36, to the phase error in the first-order-iono-free model is shown as a function of elevation for quiet and active days in Figure 4 and Figure 7, respectively. As with Figure 3 and Figure 6 the scale on the y-axis ranges from 0 to 50 mm. On a quiet day the third order errors due to the r1 (proportional to Ne^2) are less than 0.5 cm even at low elevation. However, on the active day the errors reach up to 3.5 cm at low elevation. The magnitude of the r1 error is comparable to those of the s term errors. The group error due to r1 is three times as large as the phase errors shown here.

By contrast, the magnitude of the r2 and r3 errors is much much smaller, as is seen from Figure 8 and Figure **11**, and Figure 9 and Figure 12, respectively. Each is a two-dimensional histogram of the error as a function of elevation. The errors on quiet days are plotted on Figure 8 (r2) and Figure 9 (r3). Figure 11 (r2) and Figure 12 (r3) are the errors on the active day. Notice that on all of these, the y-axis scale ranges up to only *0.05 mm*. The group delay errors due to r2 and r3 are three times as large as the magnitudes in these plots. In both the group and phase cases, the r2 and r3 errors are sub-millimeter. For this reason, we find that Brunner and Gu (B&G) were

justified in keeping only the q, s, and r1 terms in their model of the index of refraction.

Having estimated the magnitude of each of the higher order errors, up to the fourth power in signal frequency, we discard the sub-millimeter terms and adopt the B&G model for our subsequent analysis. We plot the total phase error arising in the FOIF model when compared to the B&G model, as given in Equation 31 and Equation 34, for the quiet day and active day, as a function of elevation. These are shown in Figure 10 and Figure 13, respectively. The scale of the y-axis reaches up to 20 cm. The magnitudes of the errors shown in Figure 10 are the sums of the individual errors shown on Figure 3 and Figure 4. On an active day, the higher order phase errors can reach up to 8 cm at low elevation, and a fraction of that on quiet days.

The total higher order group errors, given by Equation 39 in the FOIF model, are shown as a function of elevation for a quiet day in Figure 14 and for an active day in Figure 15. The y-axis scale ranges from 0 to 20 cm. These figures indicate that, based on actual data and the assumptions we have made, on an active day, the higher order group errors can reach as high as 20 cm at low elevation. On the quiet day, the errors are only about 1/6th those of the active day.

One of the primary conclusions we draw from comparing the phase errors in Figure 10 and Figure 13 to the group errors in Figure 14 and Figure 15 is that they are no longer equal and opposite. This will have an effect in smoothing of the FOIF code observable with the FOIF carrier observable.

CARRIER SMOOTHING ERRORS

In this section we examine how the higher order group and phase errors affect carrier smoothing of the code observable that is first-order-ionosphere-free (i.e. the q term has been eliminated). For this analysis we reproduce the expressions in B&H for the carrier and code 1st-order-iono-free observables, which were shown in Equation 17 and Equation 39:

$$P_{FOIF} = \rho - \frac{s}{f_1 f_2 (f_1 + f_2)} - \frac{r}{f_1^2 f_2^2}$$

Equation 44

$$L_{FOIF} = \rho + \frac{s}{2 f_1 f_2 (f_1 + f_2)} + \frac{r}{3 f_1^2 f_2^2} + B$$

Equation 45

In these expressions the true range and non-dispersive range terms are grouped together in ρ, and the integer ambiguities at each frequency are absorbed into bias B. The code is recursively smoothed with the carrier by use of a filter:

$$\hat{P}_{FOIF,i} = \frac{1}{k} P_{FOIF,i} + \frac{k-1}{k} (\hat{P}_{FOIF,i-1} + L_{FOIF,i} - L_{FOIF,i-1})$$

Equation 46

The value of k is equal to the product of the filter time constant and the data sample rate (in our case, 10 s). The smoothed estimate for the ith epoch is P-hat. It is an update of the previous estimate at epoch i-1 with a weighted combination of the current FOIF code observables P_{FOIF} and the difference between the current and most recent carrier FOIF observables, L_{FOIF}. The error is the difference between the estimate P-hat, and the range ρ:

$$\begin{aligned}
\varepsilon_i &= \hat{P}_{FOIF,i} - \rho_i \\
&= \frac{1}{k}\left(\rho_i - \frac{s_i}{f_1 f_2 (f_1 + f_2)} - \frac{r_i}{f_1^2 f_2^2}\right) \\
&\quad + \frac{k-1}{k}\left(\hat{P}_{FOIF,i-1} + \rho_i + \frac{s_i}{2 f_1 f_2 (f_1 + f_2)} + \frac{r_i}{3 f_1^2 f_2^2} + B\right) \\
&\quad + \frac{k-1}{k}\left(-\rho_{i-1} - \frac{s_{i-1}}{2 f_1 f_2 (f_1 + f_2)} - \frac{r_{i-1}}{3 f_1^2 f_2^2} - B\right) - \rho_i \\
&= \frac{1}{k}\left(-\frac{s_i}{f_1 f_2 (f_1 + f_2)} - \frac{r_i}{f_1^2 f_2^2}\right) \\
&\quad + \frac{k-1}{k}\left(\varepsilon_{i-1} + \frac{s_i - s_{i-1}}{2 f_1 f_2 (f_1 + f_2)} + \frac{r_i - r_{i-1}}{3 f_1^2 f_2^2}\right)
\end{aligned}$$

Equation 47

The last lines of Equation 47 show that errors due to higher order terms arising in the smoothed estimate happen due to 1) large higher order group errors, and 2) large rates of change in the higher order phase errors. To examine the effect of each of these, we select lines of sight from the active day that exhibited large magnitudes of group errors and phase error rates.

The plots in Figure 16 illustrate the effect of higher order group errors in the carrier smoothed estimate error. On 29 October 2003, the higher order group errors on the line of sight (LOS) between the WAAS station in Fort Worth, Texas, and GPS SVN 32 built up to nearly 20 cm as the satellite rose and set in the sky. This station-satellite pair produced some of the highest errors, seen at low elevation, shown as the points in the upper left region of Figure 15. The top plot (a) of shows the higher order group errors as a function of UTC hour. The y-axis scale ranges from 0 to 20 cm. The middle plot (b) shows the satellite elevation versus time. The satellite reaches nearly zenith around 18:15 UT. The bottom plot (c) shows the smoothing error given by Equation 47 that arises as a result of the group errors in plot (a) for two

different time constants that span a range of possible filter time constants for smoothing multipath. The blue curve shows the error that accumulates for a filter time constant of 100 s. The 100-second filter tracks the group errors in plot (a), reaching nearly 18 cm of error in the smoothed estimate. For a much longer time constant of 2 hours, the errors over time are significantly smaller, at only a couple cm. A longer time constant de-weights the FOIF group observable, and thus the errors associated with it, via to the 1/k term in Equation 47.

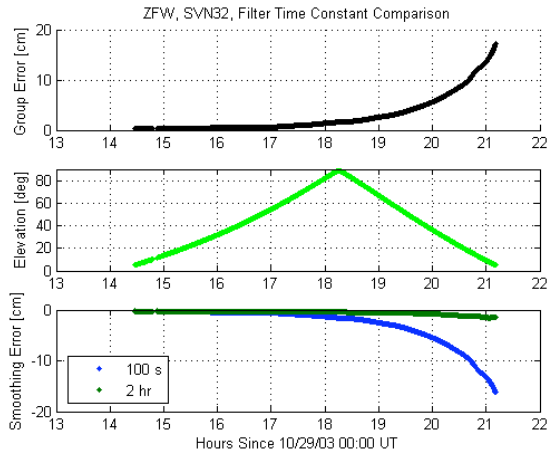

Figure 16: (a) Higher order group errors vs. time for a line of sight with particularly high errors. (b) Elevation vs. time. (c) Carrier smoothing error of the FOIF observable for a 100-s time constant (blue) and a 2-hour time constant (green).

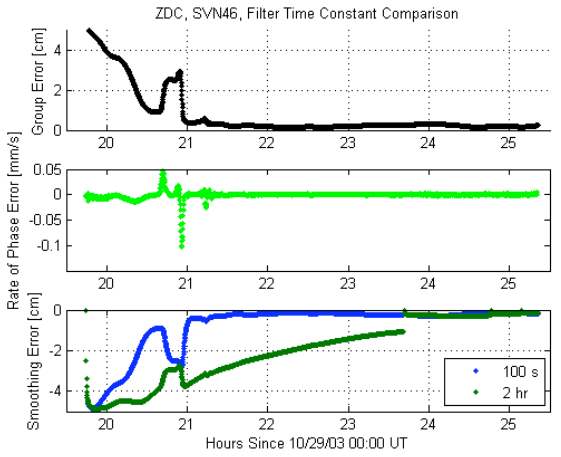

Figure 17: (a) Higher order group errors vs. time for a line of sight with particularly high phase rate of change. (b) Rate of higher order phase error vs. time. (c) Carrier smoothing error of the FOIF observable for a 100-s time constant (blue) and a 2-hour time constant (green).

Rates of change in the FOIF phase observable also contribute to the smoothing error. To examine the impact of these we choose a LOS between the WAAS station in Washington, D.C., and SVN 46. Walter et al. (2004) showed this station-satellite pair exhibited extremely high rates of change in the first-order ionosphere group delay. Since the higher order errors are proportional to the first order errors, as we found earlier, high rates of change in the first order error imply high rates of changes in the higher order errors. The plots in Figure 17 show the smoothing errors for this LOS. The uppermost plot (a) shows the higher order group error as a function of UTC hour. The scale ranges from 0 to 4 cm. The rate of change of the higher order phase error is plotted in green on plot (b). The largest magnitude phase error rate is 0.1 mm/s. Finally the smoothing error, given by Equation 47, is plotted versus UTC hour for two time constants on plot (c). The smoothing error for a 100 s filter is shown in blue and for a 2-hour filter in dark green.

The group error in (a) starts at its highest values, so both filters have almost 4 cm error in the earliest moments. The 100-s filter then decreases rapidly, tracking the group errors of plot (a). The 2-hour filter decreases much more slowly. In fact, the 2-hour filter does not reach steady state before a data outage at 23:40 UT causes the filter to reset and being smoothing a new track. In both cases the anomaly in the ionosphere group error from 20:45 – 21:00 UT is filtered in and appears in the result. For the 100 s time constant, the smoothing error (plot (c) blue curve) basically tracks the group error of plot (a) but is opposite in sign.

In the case of the 2-hour filter result, the anomaly enters the filtering process before a full two hours has even elapsed. In our implementation, the instantaneous filter constant $t_{filter,i}$ at the i^{th} epoch equals the minimum of either the target filter constant (e.g. t_{filter_final} = 2 hours) or the time elapsed since the first epoch:

$$t_{filter,i} = \min(t_{filter\_final}, t_i - t_0)$$

Equation 48

As a result, the filter constant increases with each epoch as the anomaly is filtered into the estimate. For this reason the group anomaly appears in the smoothed estimate with an amplitude that is scaled by a different value at each epoch, giving the green curve in plot (c) a different shape with respect to the original group error shown in plot (a). The phase error rate of change does not appear to have a significant impact on the error in either the 100-s or the 2-hour filtering cases.

CONCLUSION

We used WAAS supertruth data from the most recent solar maximum to compute the magnitude of each of the terms that appear in the literature, up to the negative fourth power of frequency. We found that the Brunner & Gu model, which keeps the third power of frequency and only the fourth power term that is proportional to Ne^2 is

the simplest because it neglects sub-millimeter errors. We applied the Brunner and Gu model to data to show that the higher order group errors that remain after using the dual-frequency ionosphere correction model give phase errors of up to 8 cm and group errors of up to 20 cm at low elevation on days of extreme ionospheric activity. These values are 0.06% and 0.16%, respectively, of the first order error at L1 frequency. Klobuchar (1996) pointed out that the commonly used dual frequency model is typically accurate to 0.1%. Our estimate of the higher order group errors slightly exceeds those of the simulations in the literature. We attribute this difference to the fact that, in computing the magnitude of the higher order errors, we deliberately chose the necessary simplifications such that they bounded the errors that may occur.

We showed that the higher order errors appear in carrier smoothing of the first-order-ionosphere-free code observable. The higher order group errors, and to a lesser extent the higher order phase error rates, contribute to the smoothing error. For a 100 s time constant, a low-elevation satellite with a 20 cm higher-order group delay will exhibit a 20 cm smoothing error. This can be reduced to a few cm with a longer filter time constant, as we show for a 2-hour filter. The higher order phase error rate showed no significant effects in either the 100-s or 2-hour filter estimates.

Higher order ionosphere errors of magnitude up to 20 cm may be bounded by dual-frequency augmentation systems to provide integrity in one of two ways. The higher order errors may be estimated in methods similar to the one shown in this paper and removed. Alternatively, the entire higher order error term may be bounded without removal. Whether one of these methods is better suited to wide-area or local-area differential GPS systems has yet to be determined.

ACKNOWLEDGMENTS

The authors appreciate the support of the FAA Wide Area Augmentation System (WAAS) Program, which funded this research.

REFERENCES

Bassiri, S., "Three-Frequency Ranging Systems and Their Applications to Ionospheric Delay Calibration," Telecommunications and Data Acquisition Progress Report 42-103, p. 14-20, Jet Propulsion Lab., Pasadena, California, 1990.

Bassiri, S., and G. A. Hajj, "Higher-order ionospheric effects on the global positioning system observables and means of modeling them," *Manuscripta Geodaetica*, 1993, vol. 18, p. 280-289.

Bittencourt, J. A., *Fundamentals of Plasma Physics*, 3rd ed., Sao Jose dos Campos, S.P., Brazil: J. A. Bittencourt, 2003.

Born, M., and E. Wolf, *Principles of Optics*, 6th ed., New York: Pergamon, 1980.

Brunner, F. K., and M. Gu, "An improved model for the dual frequency ionospheric correction of GPS observations," *Manuscripta Geodaetica*, 1991, vol. 16, p. 205-214.

Gu, M., and F. K. Brunner, "Theory of the two frequency dispersive range correction," *Manuscripta Geodaetica*, vol. 15, p. 357-361.

Hartmann, G.K. and R. Leitinger, "Range errors due to ionospheric and tropospheric effects for signal frequencies above 100 MHz," *Bulletin Geodesique*, vol. 58, p. 109-136, 1984.

Jackson, J.D., *Classical Electrodynamics*, 3rd ed., John Wiley & Sons: New York, 1999, p. 325.

Klobuchar, J. A., " Ionospheric Effects on GPS," *Global Positioning System: Theory and Application, Vol. I*, B. Parkinson, J. Spilker, P. Axelrad, and P. Enge (Eds.), American Institute of Aeronautics and Astronautics, pp. 485-515, 1996.

Macmillan, S., "IAGA V-MOD Geomagnetic Field Modeling: International Geomagnetic Reference Field IGREF-10," http://www.ngdc.noaa.gov/IAGA/vmod/igrf.html, revised 22 Mar 2005, accessed 8 Aug 2006.

Mannucci, A.J., B.T. Tsurutani, B.A. Iijima, A. Komjathy, A. Saito, W.D. Gonzalez, F.L. Guarnieri, J.U. Kozyra, and R. Skoug (2005), "Dayside global ionospheric response to the major interplanetary events of October 29–30, 2003 'Halloween Storms,' " *Geophys. Res. Lett.*, *32*, L12S02, doi:10.1029/2004GL021467.

Misra, P., and P. Enge, *Global Positioning System: Signals, Measurements, and Performance*, 2nd ed., Ganga-Jamuna Press: Lincoln, Massachusetts, 2006.

Ross, W. J., "Second-Order Effects in High-Frequency Transionospheric Propagation," *Journal of Geophysical Research*, vol. 70, p. 597-612, 1965.

Tsyganenko, N. A., "Geopack-2005," http://modelweb.gsfc.nasa.gov/magnetos/data-based/Geopack_2005.html, 4 May 2005, accessed 8 Aug 2006.

Tucker, A.J., and B.M. Fannin, "Analysis of ionospheric contributions to the doppler shift of CW signals from artificial earth satellites," *Journal of Geophysical Research*, vol. 73, p. 4325-4334, 1968.

Walt, M. *Introduction to Geomagnetically Trapped Radiation*, New York: Cambridge University Press, 1994.

Walter, T., S. Datta-Barua, J. Blanch, and P. Enge, "The Effects of Large Ionospheric Gradients on Single Frequency Airborne Smoothing Filters for WAAS and LAAS," *Proceedings of ION NTM 2004*, San Diego, California, 26-28 January 2004, p. 103-109.

APPENDIX

The Appleton-Hartree equation describes the phase index of refraction for a right hand circularly polarized wave (i.e. extraordinary mode) propagating through the ionosphere:

$$n_\phi^2 = 1 - \frac{X}{1 - \frac{Y^2 \sin^2\theta_B}{2(1-X)} - \left(\frac{Y^4 \sin^4\theta_B}{4(1-X)^2} + Y^2 \cos^2\theta_B \right)^{1/2}}$$

Equation 49

The angle between the magnetic field and the propagation direction is θ_B, and X and Y are given by Equation 50:

$$X = \left(\frac{f_p}{f} \right)^2, \quad Y = \frac{f_g}{f}$$

Equation 50

In Equation 50, the plasma frequency is f_p, the gyro frequency is f_g, and the wave frequency is f. The plasma and gyro frequencies are defined as:

$$f_p^2 = \frac{N_e e^2}{m_e \varepsilon_0}, \quad f_g = \frac{e|B|}{m_e}$$

Equation 51

The plasma frequency is proportional to the electron number density N_e, and the cyclotron frequency is proportional to the magnitude of the magnetic field in the plasma B. The remaining terms are constants: electron charge e, electron mass m_e, and permittivity of free space ε_0.

The Appleton-Hartree equation is a beautiful closed-form expression of the dispersion relation in a cold, collisionless, magnetized plasma such as the ionosphere, but as a model for GPS ranging errors it is unwieldy. For this reason simplifications are made through a variety of approximations and Taylor expansions. The simplest is to treat the denominator of Equation 49 as equal to one:

$$n_\phi \approx (1 - X)^{1/2}$$

Equation 52

Then by treating X as a small quantity α and Taylor expanding n_ϕ about α=0 as:

$$\begin{aligned} n_\phi &\approx (1-\alpha)^{1/2} \\ &\approx n_\phi(0) + \left.\frac{dn_\phi}{d\alpha}\right|_{\alpha=0} (\alpha) + \frac{1}{2}\left.\frac{d^2 n_\phi}{d\alpha^2}\right|_{\alpha=0} (\alpha^2) + O(\alpha^3) \\ &\approx 1 + \frac{1}{2}\alpha - \frac{1}{8}\alpha^2 \end{aligned}$$

Equation 53

we arrive at the first order model for the phase index of refraction by truncating after the first two terms:

$$n_\phi = 1 - \frac{X}{2}$$

Equation 54

The group index of refraction is related to the phase index of refraction by Equation 4, giving:

$$n_\rho = 1 + \frac{X}{2}$$

Equation 55

Using each of Equation 54 and Equation 55 in Equation 1, we find that the ionosphere error on the phase I_ϕ is equal and opposite to the ionosphere error on the code I_ρ, and that these errors are inversely proportional to the square of the signal frequency through X, given in Equation 50.

This paper is concerned with using data to calculate the errors that arise by making this first order approximation. We review and reprint the main derivations of the higher order terms in the literature, since these produce exactly the quantities we use our data to compute.

Tucker and Fannin (1968) begin with Equation 49 and make a quasi-longitudinal approximation. This assumes that the magnetic field is nearly aligned with the propagation direction, such that $\sin\theta \approx 0$. This gives:

$$n_\phi^2 \approx 1 - \frac{X}{1 - |Y \cos\theta_B|}$$

Equation 56

The denominator is very nearly 1 and can be Taylor expanded as a function $g(\varepsilon)$:

$$g(\varepsilon) = (1-\varepsilon)^{-1}$$
$$\approx g(0) + \left.\frac{dg}{d\varepsilon}\right|_{\varepsilon=0}(\varepsilon) + \frac{1}{2}\left.\frac{d^2g}{d\varepsilon^2}\right|_{\varepsilon=0}(\varepsilon^2) + O(\varepsilon^3)$$
$$\approx 1 + \varepsilon + \varepsilon^2$$

Equation 57

This gives an expression for index of refraction:

$$n_\phi \approx (1 - X(1 + Y\cos\theta_B + Y^2\cos^2\theta_B))^{1/2}$$

Equation 58

By treating the second, third, and fourth terms as a small quantity α, we again make use of the expansion in Equation 53. Keeping only the terms that are up to the fourth power in frequency f, we arrive at the Tucker and Fannin model:

$$n_\phi = 1 - \frac{1}{2}X - \frac{1}{2}XY\cos\theta_B - \frac{1}{8}X^2 - \frac{1}{2}XY^2\cos^2\theta_B$$

Equation 59

With slight modification this same derivation can be used to obtain the Brunner and Gu (1991) model. Returning to Equation 57 and keep only the 0th and 1st order terms in ε, the expression for n_ϕ becomes not Equation 58, but rather:

$$n_\phi \approx (1 - X(1 + Y\cos\theta_B))^{1/2}$$

Equation 60

As before, treating all of the terms in Equation 60 containing X as small quantity α, we use Equation 53 and drop any term that is higher than fourth power in frequency to obtain:

$$n_\phi = 1 - \frac{1}{2}X - \frac{1}{2}XY\cos\theta_B - \frac{1}{8}X^2$$

Equation 61

Although this is the Brunner and Gu (B&G) model, they point out that they derive this model without making the quasi-longitudinal approximation of Equation 56. Their preferred route is to analyze the order of magnitude of the terms to derive the expression. We summarize their argument here.

B&G begin by multiplying the numerator and denominator in Equation 49 through by (1-X). This gives a different form of the Appleton-Hartree equation:

$$n_\phi^2 = 1 - \frac{X(1-X)}{1 - X - \frac{1}{2}Y^2\sin^2\theta_B - \left(\frac{1}{4}Y^4\sin^4\theta_B + Y^2\cos^2\theta_B(1-X)^2\right)^{1/2}}$$

Equation 62

Defining everything other than the first term in the denominator as ε and using the expansion in Equation 57 up to first order only, the refractive index becomes:

$$n_\phi^2 \approx 1 - X(1-X)\left\{1 + X + \frac{1}{2}Y^2\sin^2\theta_B + \left[\frac{1}{4}Y^4\sin^4\theta_B Y^2\cos^2\theta_B(1-X)^2\right]^{1/2}\right\}$$
$$\approx 1 - X\left\{(1-X)\left(1 + X + \frac{1}{2}Y^2\sin^2\theta_B + \left[\frac{1}{4}Y^4\sin^4\theta_B + Y^2\cos^2\theta_B(1-X)^2\right]^{1/2}\right)\right\}$$

Equation 63

By treating everything except the first term as quantity α, the expansion in Equation 53 can again be used. However, their consideration before applying Equation 53 is that since $n_\phi^2 \sim \alpha$ in that equation, $\delta\alpha = 2\delta n_\phi$. Since mm accuracy is needed in the higher order terms, only the terms in the refractive index of accuracy up to 10^{-9} are needed. Since X is on the order of 10^{-5} for GPS frequencies, the only terms inside the curly brackets that need to be kept are the ones of order 10^{-4}. Using the order of magnitude value of $Y \sim 10^{-3}$, this gives:

$$n_\phi^2 \approx 1 - X\left\{(1-0)\left(1 + 0 + 0 + \left[0 + Y^2\cos^2\theta_B(1-X)^2\right]^{1/2}\right)\right\}$$
$$\approx 1 - X\{1 + Y\cos\theta_B(1-0)\}$$
$$\approx 1 - X\{1 + Y\cos\theta_B\}$$

Equation 64

All of the terms in Equation 63 that were negligible by this argument are shown as zeros in Equation 64. Notice that the final result is equivalent to Equation 60 and thus leads to the B&G model shown in Equation 61.

Finally, we show the model for refractive index obtained by Bassiri and Hajj (1993). Beginning from Equation 49 and comparing the two terms within the square root, they use the argument that $Y << 2|\cos\theta_B|(1-X)/(\sin^2\theta_B)$ to neglect the first term in the square root:

$$n_\phi^2 \approx 1 - \frac{X}{1 - \frac{Y^2\sin^2\theta_B}{2(1-X)} - Y\cos\theta_B}$$
$$\approx 1 - \frac{X(1-X)}{1 - X - \frac{1}{2}Y^2\sin^2\theta_B - Y\cos\theta_B}$$

Equation 65

Again we treat everything except the first term in the denominator as ε and approximate the denominator with Equation 57, keeping only the terms up to the fourth power in frequency f. This results in:

$$
\begin{aligned}
n_\phi^2 &\approx 1 - X(1-X)[1 + X + \frac{1}{2}Y^2 \sin^2\theta_B - XY\cos\theta_B \\
&\quad + (X + \frac{1}{2}Y^2 \sin^2\theta_B + Y\cos\theta_B)^2] \\
&\approx 1 - X - \frac{1}{2}XY^2 \sin^2\theta_B - XY\cos\theta_B \\
&\quad - X(X + \frac{1}{2}XY^2 \sin^2\theta + Y\cos\theta)^2 \\
&\equiv 1 - \alpha
\end{aligned}
$$

Equation 66

Defining everything except the first term as α, we substitute this form of α into Equation 53, and again retain terms up through the fourth power in frequency:

$$
\begin{aligned}
n_\phi &= 1 - \frac{1}{2}X - \frac{1}{4}XY^2 \sin^2\theta - \frac{1}{2}XY\cos\theta \\
&\quad - \frac{1}{2}XY^2\cos^2\theta - \frac{1}{8}X^2 \\
&= 1 - \frac{1}{2}X - \frac{1}{2}XY\cos\theta - \frac{1}{8}X^2 \\
&\quad - \frac{1}{4}XY^2(\sin^2\theta + 2\cos^2\theta) \\
&= 1 - \frac{1}{2}X - \frac{1}{2}XY\cos\theta - \frac{1}{8}X^2 \\
&\quad - \frac{1}{4}XY^2(1 + \cos^2\theta)
\end{aligned}
$$

Equation 67

The final expression is the index of refraction approximation shown in Bassiri and Hajj (1993).